

# Initial Cumulative Effects in Femtosecond Pulsed Laser-induced Periodic Surface Structures on Bulk Metallic Glasses

Chen Li<sup>1,2,3</sup>, Hao Zhang<sup>1</sup>, Guanghua Cheng<sup>2</sup>, Nicolas Faure<sup>1</sup>, Damien Jamon<sup>1</sup>, Jean-Philippe Colombier<sup>1</sup> and Razvan Stoian<sup>1</sup>

<sup>1</sup> *Laboratoire Hubert Curien, UMR 5516 CNRS, Université de Lyon, Université Jean Monnet, 42000 Saint Etienne, France*

*E-mail: razvan.stoian@univ-st-etienne.fr*

<sup>2</sup> *State Key Laboratory of Transient Optics and Photonics, Xi'an Institute of Optics and Precision Mechanics, CAS, Xi'an710119, Shaanxi, China*

<sup>3</sup> *University of Chinese Academy of Science, Beijing 10049, China*

We investigate initial cumulative irradiation effects leading to variable surface topographies and nanoscale roughness, and triggering eventually the formation of laser-induced periodic surface structures (LIPSS) on Zr-based bulk metallic glasses ( $\text{Zr}_{41.2}\text{Ti}_{13.8}\text{Cu}_{12.5}\text{Ni}_{10}\text{Be}_{25.5}$  (at%)). We discuss interconnected aspects related to electronic excitation and optical transients, potential variations in the cartography of thermally-driven chemical modifications and topographical features assisting the surface coupling of the electromagnetic field. The transient optical properties of Zr-based BMG surfaces upon ultrafast irradiation, measured by a two-angle time-resolved single-pump double-probe ellipsometry method, show a remarkable constancy up to the point of optical damage and rapid gas-phase transition beyond. In intermediate and low exposure conditions, in the vicinity of the damage domain, multi-pulse incubation effects determine the appearance of nanoscale surface structures. The aspects discussed here involve primarily the progression of nanoscale structuring with an increasing number of fs laser pulses starting from a rough surface and evolving towards ordered corrugation. We emphasize the role of initial roughness in determining light coupling and the generation of regular stationary patterns of scattered light, localized energy absorption and spatially-variant ablation or modulated temperature-driven factors for surface relief. From a material perspective, energy dispersive X-ray spectrometry (EDX) analysis shows potential selective vaporization of light elements, leading to gradual compositional changes and proving a spatially-modulated temperature pattern. A formation scenario is proposed involving interference between the incident laser and scattered light potentially mediated by localized surface plasmons. Finite-difference time-domain (FDTD) simulations are applied to validate the mechanism, showing that LIPSS appear intrinsically related to the surface superposition of electromagnetic waves.

DOI: 10.2961/jlmn.2016.03.0014

**Keywords:** LIPSS, ultrafast laser processing, Zr-based BMG, EDX, FDTD, LSP

## 1. Introduction

Femtosecond laser irradiation is a powerful tool for material processing, extendable to almost all solid materials, such as metals, semiconductors, dielectrics, polymers, or biological tissues. A variety of precise micro-scale and nano-scale structures can be fabricated by ultrashort pulsed laser ablation of surfaces, given its ability to localize energy on scales similar to the radiation wavelength. A prominent example is the spectacular appearance of laser induced periodic surface structures (LIPSS) seen as a grating-like damage on the material surface irradiated with spatially and temporally coherent sources. Observed almost 50 years ago [1], they are today subject of increased attention due to a number of scientific and technological reasons, among them their universality and ability to localize energy below the optical wavelength or the prospect of advanced surface engineering for performing novel functions in the mechanical and optical domains. LIPSS are generally scaling with the laser wavelength, though several classes of periodicities are observed [2-10], and mostly respond and align according to the direction of

the exciting electric field. The formation mechanism of LIPSS and their similitude with nanopatterns generated by other forms of irradiation (e.g. ion beams [11]) or with natural upscaled phenomena is still under debate, putting forward the challenge of bringing together coherent irradiation-related features and non-coherent growth mechanisms and material movement. Several mechanisms were suggested to explain the formation of LIPSS, including probably the most comprehensive approach - the generalized scattering and interference (Sipe) model [3], optical transients models coupled to the scattering approach [4], plasma mediated LIPSS formation [5, 6], surface plasmon polariton (SPP) mediated LIPSS formation [7-10], or macroscopic self-organization of unstable matter [11]. They involve optical coupling via transient optical indices, the onset of scattering sources and energy deposition with the fulfillment of synchronism and conservation laws, leading eventually to an ordered material movement. A hypothesis with a large acceptance is based on the interference of the incident laser radiation with surface-scattered electromagnetic waves, which, in the case of

metals may take the form of surface plasmon polaritons [4, 9], but other forms of scattered waves are not excluded (note the existence of electromagnetic field structures “radiation remnants” in the Sipe model [3]). The role of ablation plasmas in generating parametric processes was equally speculated in explaining qualitatively the periodicities, but this view finds difficulties in matching several experimental observations, one of them being the local response to laser polarization as seen in e.g. polarization engineering and generation of azimuthal and radial orientations [2]. SPP-induced formation theory is based on the interference of the incident laser field with laser induced SPPs for metals, however, SPPs are excited under the condition of phase-matching, difficult to fulfill for flat surfaces or for a range of materials where the optical indices do not support SPP. From here appears the necessity of taking into consideration the role of residual roughness [12, 13] and, equally, its generation and evolution with laser irradiation, notably its role in assisting fulfilling momentum conservation laws for a large range of wave vectors but equally the role of individual scattering centers. From a practical view the generation of regular nanoscale patterns can have potential impact in surface engineering and treatment for novel functionalities, notably in tribology, wettability, mechanics, optics, marking and counterfeiting [14-17].

The relation between radiation patterns and the reaction of materials with engineered optical and thermo-mechanical properties may emphasize furthermore the potential of laser periodic patterns in materials of technological interests and we approach here LIPSS formation processes on amorphous metallic alloys.

Bulk metallic glasses (BMG) are solid non-crystalline metallic alloys with disordered atomic-scale structure and ideal material supports for micro geometries due to lack of crystallites, grain boundaries and dislocations in material structure. Zr-based BMG shows remarkable mechanical and chemical properties, notably high strength, large elastic strain limit, good elastic behavior, high corrosion resistance and good thermoplasticity. Consequently, this material can be used to fabricate a range of microsystems; from micro springs, micro actuators in high shock environments to RF switches [18]. Zr-based BMG with a composition  $Zr_{41.2}Ti_{13.8}Cu_{12.5}Ni_{10}Be_{25.5}$  (at%), is studied in this article. From a thermodynamic standpoint, Zr-BMG transforms from a hard and relatively brittle state to rubber-like state with low viscosity, when heated to the glass transition temperature of  $T_g=623$  K. The material starts to produce crystalline phases of  $Zr_2Cu$  and  $ZrBe_2$  from the non-crystalline metallic alloy when it is heated to the crystallization temperature  $T_x=705$  K. The melting point of Zr-based BMG is 932 K. The alloy could be used for large scale fabrication of micro-systems by the thermoplastic forming method, which involves heating the BMG in temperature domains ranging between  $T_g$  and  $T_x$  under an applied pressure [18]. The facility of thermoplastic forming may impact LIPSS production on Zr-based BMG.

Motivated by these features, we focused on Zr-based BMG as the investigation material in observing the initial LIPSS formation steps from a topological and compositional viewpoint.

Subjected to ultrafast laser radiation, Zr-based metallic glass shows several particular features in generating regular patterns [19], summarized in Fig. 1. The figure shows the gradual dose-dependent transition from irregular roughness to polarization-perpendicular regular sub-micron ripples and regular over-micron spaced groove-like structures parallel to the laser polarization. Interestingly, in specific conditions such as those related for example to a low fluence (of  $0.2$   $Jcm^{-2}$  in the example below), singular cracks oriented parallel to the polarization may appear, developing upon increasing number of pulses in patterns with an odd number of traces (Fig. 1(a)), pointing out unique thermo-mechanical evolution ways. Nanoscale structures appear with the micron-sized cracks. At higher fluences (of  $0.3$   $Jcm^{-2}$ ), a more visible standard ripple pattern is observed in Fig. 1(b).

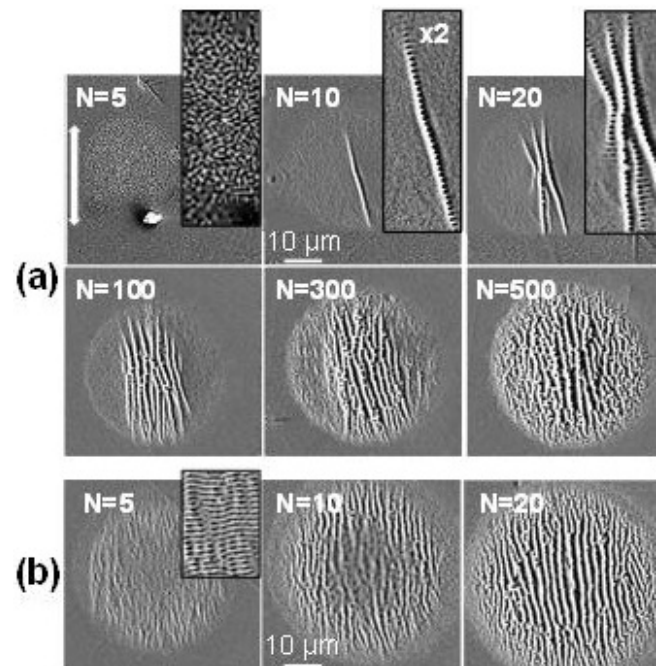


**Fig. 1** Scanning electron microscopy images of the Zr-BMG ( $Zr_{44}Ti_{11}Cu_{10}Ni_{10}Be_{25}$  (at%)) [19] surface after irradiation with a varying number of linearly polarized ultrashort laser pulses at the following fluences of (a)  $\Phi=0.2$   $Jcm^{-2}$ ; (b)  $\Phi=0.3$   $Jcm^{-2}$ . The arrow indicates the electric field direction. A range of regular structures are observed.

Observing this evolution we focus below on the role of excitation in creating initial ripple topologies and we underline the features corresponding to a ripple class with subwavelength periodicities in the vicinity of the incident wavelength. The manuscript is structured as follows. An experimental section shows the evolution of surface topographies with increasing dose. We first analyze the role of excitation transients using time-resolved ellipsometry and then pinpoint spatially-modulated energy deposition patterns using an elemental compositional check. The role of roughness in determining modulated irradiance is explained by using a Finite-difference-time-domain approach, showing the development of stationary field patterns. Single and multiple scattering sources are discussed, as well as the role of the scattered radiation in modulating energy income. A conclusion section resumes the main findings.

## 2. Experiment and Topology Analysis about Initial LIPSS Formation

The single-side polished Zr-based BMG  $Zr_{41.2}Ti_{13.8}Cu_{12.5}Ni_{10}Be_{25.5}$  sample with dimensions of  $10 \times 6 \times 3 \text{ mm}^3$  were used in the experiment.  $Zr_{41.2}Ti_{13.8}Cu_{12.5}Ni_{10}Be_{25.5}$  samples were prepared from a mixture of pure Zr, Ti, Cu, Ni and Be elements fused together in an arc-melting furnace under Ti-gettered argon atmosphere. The ingots were melted in quartz tubes, and then cooled rapidly in water to obtain BMG samples. After cutting, polishing was done by diamond paste and alumina powder with grit size down to  $0.1 \mu\text{m}$ . Amorphous samples before experiments were identified by Electron Back Scatter Diffraction (EBSD).

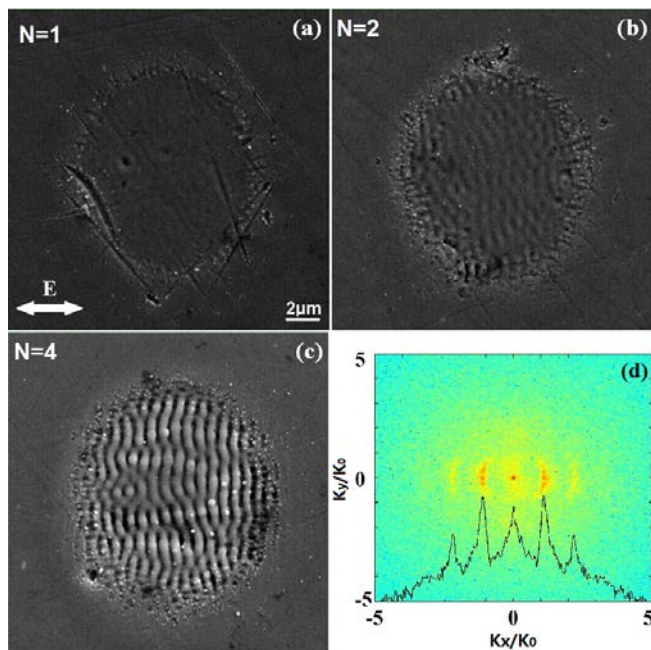


**Fig. 2** SEM images of the amorphous metal Zr-BMG surface after irradiation with linearly polarized ultrashort laser pulses at a fluence of  $\phi=0.38 \text{ J}\cdot\text{cm}^{-2}$ . The pulse numbers used in irradiation are as follows: (a)  $N=1$ ; (b)  $N=2$ ; (c)  $N=4$ ; (d) 2D-FFT of the image (c), representing the periodicity in the  $k$ -space. The electric polarization direction of the laser beam is indicated with a double-headed arrow.

Before and after laser fabrication, Zr-based BMG samples were cleaned ultrasonically in ethanol for 5 min. A regenerative Ti:sapphire oscillator-amplifier system (Legend, Coherent Inc) based on the chirped-pulsed amplification technique at a central wavelength of 800 nm with pulse duration of 50 fs and repetition rate of 1 kHz was used to perform the experiments. The linearly polarized Gaussian laser beam was focused with a convex lens of focal length 100 mm. The laser fluence was adjusted by using the combination of a waveplate and a polarizer. The laser fluence is chosen at  $0.38 \text{ J}/\text{cm}^2$ , which is above the single-pulse ablation threshold on BMG of about  $0.3 \text{ J}/\text{cm}^2$ . The number of pulses is controlled by a laser shutter. Less than 5 pulses are used to investigate the initial LIPSS formation. The sample was mounted on a computer-controlled XYZ translation stage with a spatial resolution of 125 nm and the irradiated zone was observed in real time by a magnifying imaging system and projected

on a CCD monitor. All experiments were performed in ambient atmosphere with sample surface perpendicular to the propagating direction of laser beam [20, 21]. The morphology and the chemical composition of the surface on Zr-based BMG after fs laser ablation were analyzed using scanning electron microscopy (SEM) and energy dispersive X-ray spectrometry (EDX).

We follow first the topology changes upon the accumulation of first incident pulses. Fig. 2 shows SEM images of LIPSS formed on the amorphous metal surface with increasing pulse number ( $N$ ) by linearly polarized laser radiation at a fixed fluence  $\phi=0.38 \text{ J}\cdot\text{cm}^{-2}$ . For  $N=1$ , we observe the circular fingerprint of laser modification, with a slight residual damage accumulating towards the edge of the irradiated spot. Regular LIPSS are not yet noticed [Fig. 2(a)]. This indicates two local fluence action ranges, with different roughness topologies according to the Gaussian pulse profile. For  $N=2$ , faint ripples are observed within the irradiated spot [Fig. 2(b)]. For  $N=4$ , clear rippled pattern with orientation perpendicular to the laser polarization appears [Fig. 2(c)]. Fig. 2(d) shows 2D-Fast Fourier Transform (FFT) of Fig. 2(c) equivalent to a description in the space frequency domain that confirms a quasiconstant periodicity centered at  $730 \pm 40 \text{ nm}$ .

## 3. The Transient Optical Properties of Zr-based BMG

The transient optical properties of Zr-based BMG samples upon ultrafast irradiation were probed at 800 nm-wavelength (1.55 eV photon energy) at various fluences using a two-angle one color time-resolved ellipsometry method following the technique proposed in Ref. [22]. The static properties of the non-excited  $Zr_{41.2}Ti_{13.8}Cu_{12.5}Ni_{10}Be_{25.5}$  were first evaluated ex-situ by using a commercial ellipsometer (Uvisel, Horiba Jobin Yvon). Under 800 nm-wavelength irradiation, the refractive index of  $Zr_{41.2}Ti_{13.8}Cu_{12.5}Ni_{10}Be_{25.5}$  is  $\tilde{n}=2.27+3.34i$ . A second laser system with a pulse duration of 150 fs was used.

Fig. 3(a) shows the schematic diagram of single-pump double-probe reflectometry setup. The s-polarized pump pulse of 150 fs arrives at normal incidence on the sample surface and excites the electronic system, potentially leading to transient reflectivity changes. The 150 fs 800 nm low energy non-perturbing double probes at p-polarization allow to measure reflectivity changes at two different incident angles  $\theta_1=28.7^\circ$  and  $\theta_2=65.8^\circ$  at the same time, which allows for the recovery of changes in the real and imaginary part of the refractive index  $\tilde{n}=n+ik$ . The double probe pulses arrive at a controllable time delay with respect to the pump. The superposition of the three laser spots on the sample is monitored by a CCD-camera via a  $20\times$  zoom objective. The probed zone is significantly smaller than the spatial extent of the pump excited region and therefore ensures that the smaller probe beam measures a uniformly excited region of the sample. Two photodiode detectors positioned in imaging geometries with respect to the surface are used to measure the probe reflectivities. In order to minimize scattered light from the s-polarized pump pulse, high-contrast polarizers are used before the two photodiode detectors. To minimize the influence of fluctuations in the laser energy, another reference

photodiode detector is used to measure the fluctuations of laser pulse chain. The measured values of the transient reflectivity changes are recorded and the corresponding refractive index ( $n$ ,  $k$ ) with different delay times are obtained by inverting Fresnel formulas at the given angles. Two fluence domains were used, a low fluence range below the multipulse ablation threshold where all data were recorded on the same spot as no cumulative changes take place, and a high fluence range, above the single-pulse ablation threshold, where fresh spots were used for every pulse, with sample movement. The accuracy of the measurement is affected by the roughness and local planarity of the surface. The measurement results are shown in Fig. 3(b-g).

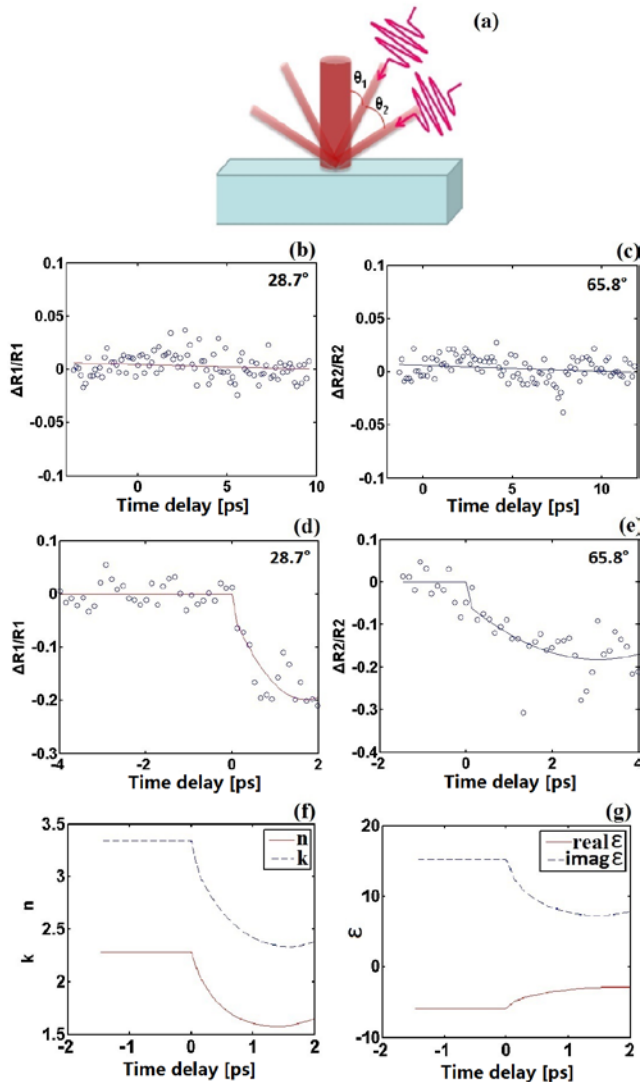


**Fig. 3** (a) Schematic diagram of the time-resolved ellipsometry/reflectometry setup. (b-e) Two-angle time-resolved reflectivity changes of the surface upon normal ultrafast laser irradiation in two fluence regimes: (b,c) Changes of excited surface reflectivity at the incident angles of 28.7° and 65.8° at a pump fluence of 0.038 J/cm<sup>2</sup> below ablation threshold. (d,e) Changes of reflectivity at the incident angle of 28.7° and 65.8° at pump fluence of 1.22 J/cm<sup>2</sup>. (f) Retrieved  $n$ ,  $k$  behavior in the high fluence domain from (d,e). (g) Retrieved behavior of real and imaginary parts of  $\epsilon$  in the high fluence domain from (d,e). Note that the decrease in  $n$  and  $k$  signalizes a fast onset of a low density plasma phase.

Several features can be outlined. Fig. 3(b,c) shows the changes of reflectivity in one spot from probe 1 and probe 2 under pump fluence of 0.038 J/cm<sup>2</sup> nearly below the multi-pulse ablation threshold (approximately 0.04 J/cm<sup>2</sup>). The reflectivity is remarkably stable upon excitation. Because the reflectivity measuring error is about 3%, including laser fluctuation and photodiode noise, therefore the complex refractive index ( $n$ ,  $k$ ) is considered to be quasi constant within the error and experimental tolerance range. This can be seen as a consequence of the multi-metal composition which should lead to a multitude of electronic states and a quasi-continuum density of states (DOS), where the effect of laser-induced electronic population/depopulation seems minimal. This behavior seem to prolong above the multishot damage threshold but below the single pulse modification threshold, however in this range incubation effects are to be expected.

Fig. 3(d,e) shows the changes of reflectivity in a higher pump fluence regime from probe 1 and probe 2 under pump fluence of 1.22 J/cm<sup>2</sup>. Different spots for each delay time on the fresh surface were used via the movement of sample. Both reflectivities at the two angles decreased significantly. The transient refractive index ( $n$ ,  $k$ ) and dielectric function components extracted from Fig. 3(d,e) are shown in Fig. 3(f) and (g) respectively. Despite the fact that the inversion assumes a flat surface, a condition which may not be fulfilled for high fluences, we note the qualitative decrease of  $n$  and  $k$ , indicating the fast appearance of a lower density plasma phase.

#### 4. Chemical Composition Analysis along the Ripples Pattern

Generally it is assumed that ripple formation is preceded by spatially modulated heating of the material according to the irradiation pattern. Thus selective ablation, vaporization or material transformation features may become observable. We have used energy dispersive X-ray spectrometry (EDX) as an analytical technique for the elemental analysis within the ripples relief. A line was scanned across the ripples from the non-ablated regions to the ablated regions for retrieving EDX data, shown in Fig. 4(a), and Fig. 4(b) gives the cross section of the ripples along the line. Fig. 4(c) shows that relative chemical composition changes along the ripples pattern (given here for two elements). Despite the penetration depth which prevents the technique of being highly surface sensitive, several features are becoming apparent.

EDX results indicate that elements seem to change in relative concentration along the ripple relief. We concentrate here on the behavior of Be and Zr for reasons related to their different thermal characteristics as it will be seen below. We note however the difficulty of measuring light elements (such as Be) in EDX. With some precautions we can make the following observations. Be shows the largest variations and Zr changes in opposite phase, appearing with a smaller yield. In the valley of the ripple pattern, Be concentration seems lower. It is noticed that not every bottom in ripple profile shows Be loss (profile valley), because of the inhomogeneous distribution of elements and relatively imperfect shape of ripples. Applying EDX on non-flat surfaces, i.e. with relief topologies of tens of nm may induce measurement errors.

Assuming that the measurement errors from ripples are similar in phase for various elements at the same location, and cannot induce the signals with opposite change trends, we may conclude that, in spite of measurements uncertainty, Be signal shows the changes of alloy composition along the ripple.

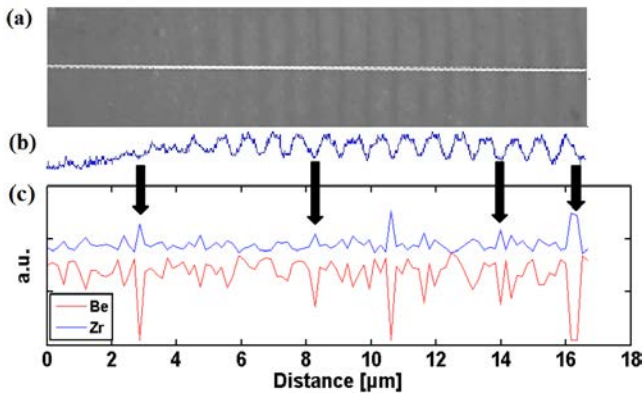


**Fig. 4** (a) SEM photo of the ripple scanned along the line for EDX; (b) the shape of cross section of the ripples along the line; (c) Relative change of Be and Zr elements along the scanned line in the ripple.

A quick look at the thermal properties of pure metals shown in Table 1 indicates that Be is easiest to be vaporized among the five metallic elements as opposed to Zr. Even if superficial vaporization is not triggered at the boiling temperature, the table gives an indication on the facility of gas-phase transformation. The low thermodynamic points of Be are accompanied by a relatively high vapor pressure and light mass. So elemental separation can be qualitatively explained eventually by a probable involvement of selective vaporization in the fs multiple-pulse ablation. Fs laser ablation on Zr-based BMG could induce therefore a potential phase separation due to selective vaporization of various elements. This spatially variable elemental mapping is a strong argument of a spatially modulated temperature profile which seems not to change once a corrugation pattern is formed. This spatial distribution of absorbed energies would depend on the topography of the surface.

**Table 1** The boiling temperature at vapor pressure 100 kPa for various elements composing the alloy [23]

Element	Temperature (K)
Zr	4678
Ti	3558
Ni	3184
Cu	2834
Be	2742

When the laser pulse energy is at the level of the single-pulse ablation threshold, the first laser pulse incident on a flat surface can damage the surface in a localized inhomogeneous manner at the sites of intrinsic surface defects or induce local nucleation of phase transformations [24]. Therefore nanostructures on the surface appear in a dominantly random manner, as seen in Fig. 2(a). The

ablative features follow generally the main characteristic of an ultrafast ablation process with rapid, quasi-isochoric heating, build-up of temperature and pressure gradients and thermomechanical relaxation with thermodynamic evolutions below or beyond the critical point [25]. If this scenario typically determines homogeneous excitation along the skin depth and stoichiometric removal, it is not excluded that a certain elemental segregation according to characteristic boiling temperatures, mass, and vapor pressures occurs. As indicated before, Be has a rather low boiling temperature and a relatively high vapor pressure, having also the lightest mass among the five composing elements, so it can happen that Be is more efficiently vaporized. After multi-pulses, the change of chemical composition is noticeable, as shown in Fig. 4(c).

However the main consequence of irradiation is the departure from a flat surface and the onset of nanoscale and compositional relief. Relying on surface nanostructures and their scattering strength, a far-field component of interference between the scattered light and incident laser can cause periodic energy modulation on the surface becoming thus a potential source for ripples [3, 12, 26, 27]. In addition, the thermoplastic formation under high temperature and high pressure in a spatially modulated energy pattern may play an important role in the ripple formation and particularly in their morphological appearance on Zr-based BMG. For example, above the glass transition temperature, thermoplastic BMG with lower viscosity becomes moldable and easier to change surface morphology, as seen in Fig. 2.

We follow below potential sources and geometries of field interference at the surface.

## 5. Energy Modulation Induced by Single Surface Nanostructure

In order to investigate the effect of surface nanostructures in LIPSS formation scenarios, we first analyze the energy modulation induced by single surface nanostructure using Finite-difference time-domain simulations. Then, the space periods and patterns of energy modulation are evaluated. To assess conductor and isolator roles of nanoprotuberances and nanoholes and emphasize their specific scattering features, simulations were carried on Zr-based BMG and dielectric material silica glass models. Finally, near-field enhancement of localized surface plasmon is discussed.

FDTD method can simulate light propagation, scattering and diffraction phenomena by solving Maxwell's equations numerically. The method was introduced by Yee in 1966 [12] and since then has been a powerful engineering tool for integrated and diffractive optics device simulations. In this article, FDTD method is used to compute the inhomogeneous electric field distribution on the surface. The surface is irradiated at normal incidence in air with linearly polarized laser pulses of 50 fs duration FWHM at 800 nm central wavelength. Because dielectric constants of Zr-based BMG change little during the laser pulse duration of 50 fs at low laser fluence and the linear response is investigated, the refractive index of  $Zr_{41.2}Ti_{13.8}Cu_{12.5}Ni_{10}Be_{25.5}$  is  $\tilde{n}=2.27+3.34i$  in FDTD simulation. Perfectly matched layer method was used as absorbing boundary condition.

In order to investigate energy modulation induced by single nanostructure, effects of single hemisphere form placed on planar surface of BMG are analyzed by 3D-FDTD simulation. In the model geometry in Fig. 5, a hemisphere with the radius of  $0.1\ \mu\text{m}$  is located in the coordinate origin. BMG planar surface is at  $Z=0$ . The incident plane wave propagates along  $Z$  axis from the source plane. The laser polarization is along  $X$  axis. The amplitude of laser pulse is set to 1. Total-field scattered-field method is used to analyze the scattered field [28]. We recall that the polarization vector of the plane wave polarization is defined along  $E_x$ , and thus the electric field  $E_x$  represents the total field. Upon interaction, newly developed electric field  $E_z$  components only include the scattered field.

The result in Fig. 5(b) shows the time-averaged  $E^2$  around the BMG hemisphere placed on BMG planar surface for one pulse duration of 50 fs in the XOZ plane. The interference between scattered light and incident laser field takes place in the space between the source plane and the surface. The electric field energy distribution arranges stationarily in a regular interference pattern and the periodic energy modulation appears on the surface. The 1D-FFT of energy modulation on surface is shown in the inset of Fig. 5(b), which shows that the spacing period is  $727\pm 20\ \text{nm}$ . The period depends slightly on the geometry of the nanoparticle on surface.

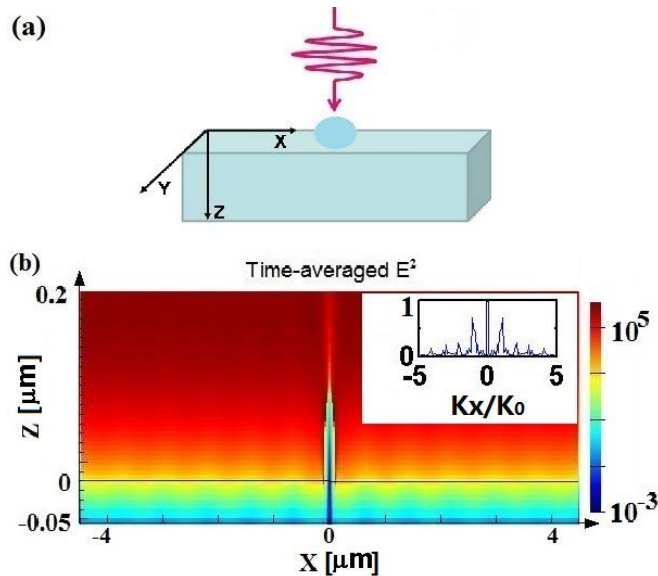


**Fig. 5**(a) Schematic geometry of interaction. (b) Time-averaged  $E^2$  values determined by a BMG hemisphere (radius= $0.1\ \mu\text{m}$ ) on the BMG surface in the XOZ plane. 1D-FFT of  $E^2$  values on surface is inserted in Fig. 5(b) showing periodic features. A logarithmic color bar scale was used to emphasize the details. Note that  $X$  axis and  $Y$  axis are in different scales.

To assess conductor and isolator roles and emphasize their specific scattering features, the energy modulation on two materials: Zr-based BMG and silica glass is analyzed by FDTD simulations respectively. The energy modulation is induced by contributions of metallic and dielectric scattering centers, equivalent to protuberances and nanoholes in the surface. The same hemisphere model as in Fig. 5 is used in 3D-FDTD simulation. To emphasize the

linear response, the dielectric constants of silica in non-excited state are chosen. In FDTD simulation, the refractive index of silica glass is  $\tilde{n}=1.45+0i$  under  $800\ \text{nm}$ -wavelength irradiation.

As the size of the surface nanostructure is comparable to the wavelength of the laser, the scattering light can be associated with Mie scattering, but we observe here a general scattering and interference phenomenon involving incident and scattered fields. The results are analyzed and shown in Fig. 6 in terms of surface pattern distribution and field diffusion patterns.

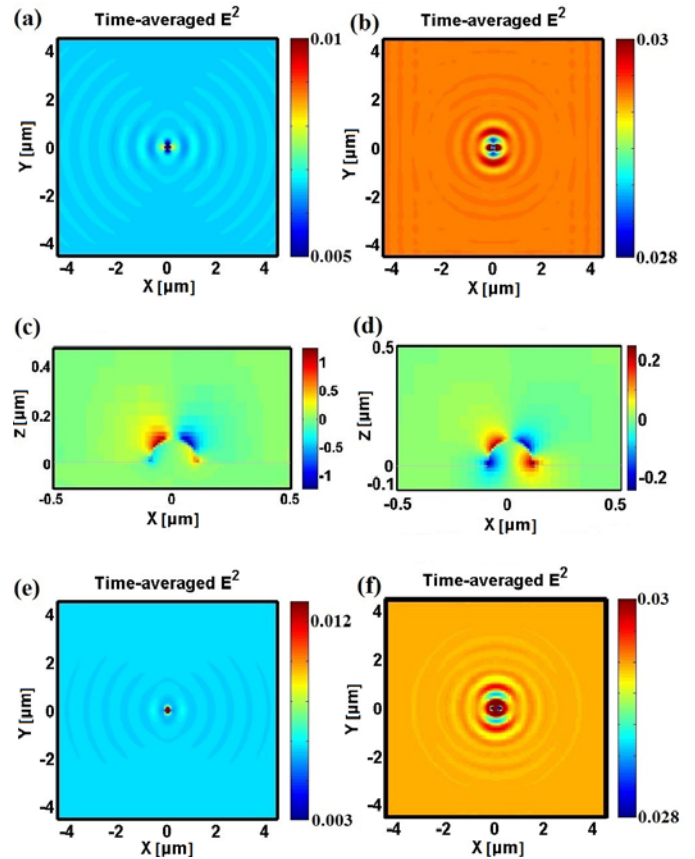


**Fig. 6**(a) Time-averaged  $E^2$  in XOY plane for a hemisphere (radius= $0.1\ \mu\text{m}$ ) on BMG; (b) Time-averaged  $E^2$  in XOY plane for a hemisphere on silica; (c) Maximum electric field  $E_z$  in XOZ plane for a hemisphere on BMG; (d) Maximum electric field  $E_z$  in XOZ plane for a hemisphere on silica. (e) Time-averaged  $E^2$  in XOY plane for a hole on BMG, (f) Time-averaged  $E^2$  in XOY plane for a hole on silica.

Time-averaged  $E^2$  distributing on surface in XOY plane for the case of BMG material illuminated by  $800\ \text{nm}$  planewave is given in Fig. 6(a). This shows a stationary spatially modulated pattern. Time-averaged electric field magnitude  $E^2$  distribution is ripple-like shaped along the polarization direction and the spacing period is  $727\pm 20\ \text{nm}$ . It is now of interest to observe the near-field diffusion pattern. Fig. 6(c) shows the peak electric fields  $E_z$  in the XOZ plane. We note that maximum  $E_z$  is 1.25, higher than the incident laser field magnitude, indicating an enhancement mechanism. To verify to which extent this is related to the material properties, particularly to the conductive characteristics which may enable collective charge oscillations or to the geometry, we verify the

situation in case of a dielectric medium. Fig. 6(b) shows time-averaged  $E^2$  distribution on surface in the XOY plane for a silica hemisphere of same size located on silica material and excited by a planewave. Time-averaged  $E^2$  distribution is a mix of patterns with two periodicities given by distributed fields above and below surface; the central spacing periods are 571 nm, 727 nm respectively. The period of 571 nm is related to the interference between the refracted wave in silica glass and scattered light. The period of 727 nm is related to the interference between incident plane wave and scattered light on the top of the surface. We thus observe space period and pattern of energy modulation dependent on substrate materials. Fig. 6(d) shows electric fields  $E_z$  in XOZ plane. The maximum  $E_z$  value is 0.25 in this case.

For comparison with hemispheres on surface, the energy modulations by nanoscale air holes on BMG and silica are also investigated by 3D-FDTD simulation. In the same model conditions as in Fig. 6(a) and 6(b), instead of a hemisphere, an air sphere is considered, that has the radius of 0.1  $\mu\text{m}$  and its center placed on the surface. The results are given in Fig. 6(e,f). Fig. 6(e) gives the time-averaged  $E^2$  in the XOY plane for a hole on BMG, which shows the same pattern as in Fig. 6(a). Fig. 6(f) shows time-averaged  $E^2$  in the XOY plane for a hole on silica, which shows the same pattern as in Fig. 6(b). We may conclude that the nanoscale particles or holes on surface play the same role in energy modulation on surface induced by interference between incident laser and scattered light. Note that the maximum  $E_z$  in metal BMG is stronger than the maximum  $E_z$  in dielectric material silica glass, as seen in Fig. 6(c) and 6(d). Such near-field enhancement can likely involve localized surface plasmons (LSP) on metal, namely non-propagating conduction electronic oscillations coupled to the electromagnetic field [29]. LSP are typical products of light excitation of small structure with free mobile electrons and resonant excitation can determine locally field amplification.

The characteristic patterns in Fig. 6(a) and near-field enhancement in Fig. 6(b) represent potential evidence that LSP excitation occurs on the BMG hemisphere under laser irradiation. LSP enhances the electric field in the near-field zone of BMG hemisphere surface, amplifying thus the yield of scattered light and influencing the energy modulation on surface.

## 6. LIPSS Formation

Based on the results on single scattering centers, we can discuss field scattering impact on low spatial frequency LIPSS formation. The N-dependence of the surface topology upon irradiation indicates cumulative effects that can be resumed as follows. When the first few pulses impact on a flat metal surface with low roughness, a certain distribution of sub-wavelength surface structures, such as nanoscale hemispheres and nanoscale holes, will be generated. The origin of these structures can be associated with inhomogeneous distributions of phase-transition nucleation centers [30]. A sub-wavelength surface metallic structure upon irradiation can scatter light assisted by potentially excited LSPs and act as a dipole source. An interference phenomenon between the incident field and the scattered field occurs, with the onset of regular patterns

at the typical wavelength of ripples. The modulated energy deposition can thus contribute to generation of LIPSS.

In order to evaluate the interaction between multiple dipole sources, cases including two and multiple BMG hemispheres on a planar surface are analyzed by FDTD simulations. In the simulation models, BMG hemispheres on planar surface have the same radius of 0.1  $\mu\text{m}$ . The incident plane wave with 800 nm wavelength propagates along the Z axis, and the polarization lays parallel to the X axis. Simulation results are shown in Fig. 7 and 8.

Fig. 7(a) shows the time-averaged  $E^2$  distribution induced by two hemispheres separated by a distance of 4  $\mu\text{m}$ . We observe already the superposition of the two individual patterns, leading to the onset of quasi-parallel periodically aligned traces at the intersection point.

Because the electric field of incident plane wave is defined in the x-axis:  $E_x$ , the electric field  $E_z$  components only come from the scattered field. The electric field magnitude  $E$  includes three components:  $E_x$ ,  $E_y$  and  $E_z$  and we discuss the stationary patterns associated with each of the component via the time-averaged squared component of the field, artificially assimilated to an energy-like component. Fig. 7(b) shows the time-averaged  $E_x^2$  distribution, which is similar to Fig. 7(a). Fig. 7(c) shows the time-averaged  $E_z^2$  distribution with a space period of about 400 nm, which derives from the coherent interaction between two scattering sources, as it will be justified below. Interference effects between incident wave and scattered wave are maximized in the x component, while z component is only originating from scattering.

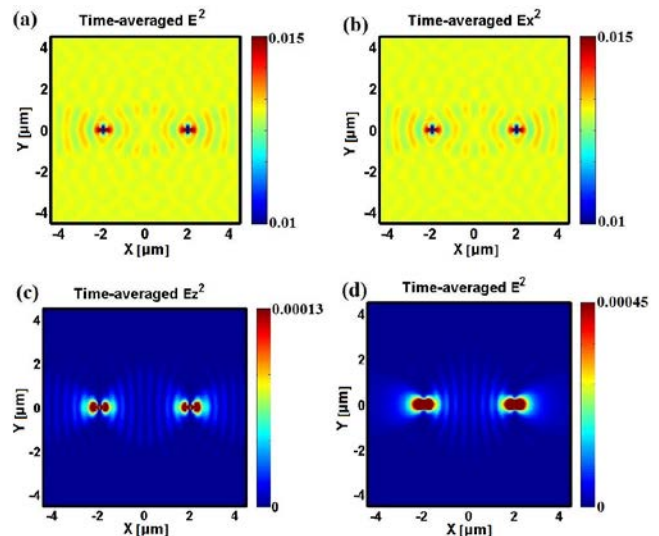


**Fig. 7**(a) Time-averaged  $E^2$  distribution induced by two laser-irradiated hemispheres (radius=0.1  $\mu\text{m}$ ) separated by the distance of 4  $\mu\text{m}$ ; (b) Time-averaged  $E_x^2$  distribution; (c) Time-averaged  $E_z^2$  distribution; (d) Time-averaged  $E^2$  distribution induced by the mutual interaction of two coherent dipole sources with the distance of 4  $\mu\text{m}$ .

In order to prove the nature of coherent effects in  $E_z$  distribution without involving interaction with the incident wave, FDTD simulation of the interaction between 2 dipole sources in the absence of the incident plane wave is performed. In this model, two dipole sources with distance of 4  $\mu\text{m}$  are located on the BMG surface as shown in Fig. 7(d). Both of the dipole sources have the electric field

amplitude of 1, the wavelength of 800 nm, the pulse period of 50 fs and the polarization along the X axis. Fig. 7(d) shows the time-averaged  $E^2$  distribution induced by the two coherent dipole sources, which is similar to Fig. 7(c) in both shape and space period. So the time-averaged  $Ez^2$  distribution arrives from the coherent interaction between two scattering sources, and shows a different periodicity than expected in low spatial frequency LIPSS. In addition, the value of time-averaged  $Ez^2$  is much lower than  $Ex^2$ , so the coherent interference between scattering sources doesn't play an important role in initial LIPSS formation in our case, a situation that may evolve as a function of scatterer concentration. The energy distribution pattern defining the regular ripples comes mainly from the interference between scattering wave and the incident laser. Comparing Fig. 7(a) with 7(b) and 7(c), we conclude that the energy modulation induced by two nanostructures comes from the interference between scattered light and incident plane wave, and also from the coherent interaction between all scattered sources, however, the interference between scattered light and incident plane wave plays a primary role in this case. This is equally emphasized by the fact that we have not yet observed fine ripple structures on BMG [31], a situation that may be related to the sized and density of features that can be obtained on a material showing plasticity.

In order to simulate the rough surface induced by a few laser pulses, the flat surface with 1000 cubic nanoparticles in random distribution on the surface is built for the FDTD simulation model [12]. The cubic particle size is  $40 \times 40 \times 40$  nm<sup>3</sup>. The surface size is  $25 \mu\text{m} \times 25 \mu\text{m}$ . The incident plane wave propagates along the Z axis. It has the wavelength of 800 nm and the polarization aligned along the X axis.

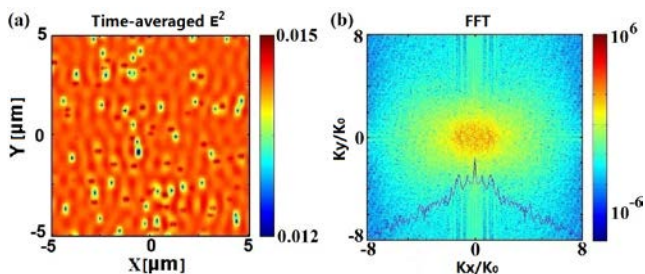


**Fig. 8**(a) Time-averaged  $E^2$  distribution just above the rough surface for an ensemble of scatterers. (b) 2D-FFT of the intensity distribution in (a), the values along  $K_y=0$  is shown at the bottom. A logarithmic color bar is used to emphasize the details.

Fig. 8 shows the time-averaged  $E^2$  for whole pulse duration just above the rough surface, and the energy modulation can be seen at this level. The energy on the surface is modulated with a pattern similar to the typical ripples, as shown in Fig. 8(a). Fig. 8(b) shows the 2D-FFT of the Fig. 8(a), from which the energy modulation distribution has the space period of  $769 \pm 20$  nm with the direction perpendicular to the laser polarization. The theoretical results agree reasonably well with that of the experiments considering that no feedback issues were considered here.

Even though FDTD is not specific to the modulation source, several points can be emphasized. The field enhancement around metallic nanostructures points to a

potential LSP involvement. The optical indices can allow SPPs propagation and Composite Diffractive Evanescent Wave (CDEW) can be excited on the Zr-based BMG [32, 33]. However a general scattering and interference model is sufficient to indicate optical modulation on the surface.

## 7. Conclusion

The initial formation steps starting with scattering centers for regular LIPSS on Zr-based BMG are investigated in this article. The transient optical properties of Zr-based BMG sample surfaces upon near-infrared ultrafast irradiation were measured by a single-color two-angle time-resolved single-pump double-probe ellipsometry/reflectometry method. Results show that at 1.55 eV the refractive index is quite robust against excitation in a fluence range below the multi-pulse ablation threshold. For laser fluences above multi-pulse ablation threshold but below the single-pulse ablation threshold BMG surface could be damaged by multi-pulse incubation effects and nanoscale surface structures appear. Well-above the single pulse threshold rapid transitions to the gas-phase appear.

The LIPSS evolutions with increasing number of fs laser pulses are experimentally observed and analyzed from a chemical composition viewpoint. EDX results show a trend for selective removal of elements along the ripple patterns, pointing out to spatially modulated temperature patterns.

Secondly the role of topology in terms of initial roughness or developing with the number of pulses is outlined. Using FDTD, we indicate interference between the scattered light and incident laser as potential cause for the periodic energy modulation on the surface contributing to regular ripple formation with the spatial periods below but in the vicinity of the wavelength. The electromagnetic calculations show the role of scattering around individual centers, indicating that the energy modulation is mainly derived from the interference between incident laser and scattered light. We indicate via a choice of materials the effect on the spacing period and pattern of energy modulation for given surface nanostructure geometries and optical nature (dielectric or metallic). For metals, LSP can be excited on surface nanostructures, enhancing the electric field in the near-field zone and light scattering.

Finally, the involvement of multiple scattering centers on the surface is analyzed by FDTD for investigating the low spatial frequency LIPSS formation. A formation scenario is thus proposed relying on interference between the incident laser and scattered light. The LIPSS periods around the wavelength in case of BMG suggest a far-field component of the interference. The FDTD simulation results agree with experimental results. Beyond interference, effects related to scattering interactions are equally proposed.

## Acknowledgments and Appendixes

The authors acknowledge the financial support from China Scholarship Council in Chinese high-level public university post-graduate project and the National Natural Science Foundation of China (No.61378019 and No.61223007). This work was also supported by French ANR project DYLISS (ANR-12-IS04-0002-01).

## References

- [1] M. Birnbaum: *J. Appl. Phys.*, 36, (1965) 3688.
- [2] R. Buividas, M. Mikutis and S. Juodkazis: *Prog. Quant. Electron.*, 38, (2014) 119.
- [3] J.E. Sipe, J.F. Young, J.S. Preston, and H.M. van Driel: *Phys. Rev. B.*, 27, (1983) 1141.
- [4] J. Bonse, A. Rosenfeld and J. Krüger: *Appl. Surf. Sci.*, 257, (2011) 5420.
- [5] O. Varlamova, J. Reif, S. Varlamov and M. Bestehorn: *Appl. Surf. Sci.*, 257, (2011) 5465.
- [6] S. Sakabe and M. Hashida: *Phys. Rev. B.*, 79, (2009) 033409.
- [7] G. Miyaji and K. Miyazaki: *Opt. Express*, 16, (2008) 16265.
- [8] J.Y. Derrien, R. Torres, T. Sarnet, M. Sentis and T.E. Itina: *Appl. Surf. Sci.*, 258 (2012) 9487.
- [9] G. Obara, Y. Tanaka, N.N. Nedyalkov, M. Terakawa and M. Obara: *Appl. Phys. Lett.*, 99, (2011) 061106.
- [10] G. Miyaji and K. Miyazaki: *Opt. Express*, 20, (2012) 148482.
- [11] O. Varlamova, J. Reif, S. Varlamov and M. Bestehorn: "Progress in Nonlinear Nano-Optics.", ed. by S. Sakabe, C. Lienau and R. Grunwald, (Springer, 2015), p.4.
- [12] J.Z.P. Skolski, G.R.B.E. Römer, J.V. Obona, V. Ocelik, A.J. Huis in't Veld and J.Th.M. De Hosson, *Phys. Rev. B.*, 85, (2012) 075320.
- [13] S.I. Ashitkov, P.S. Komarov, A.V. Ovchinnikov, E.V. Struleva, V.V. Zhakhovskii, N.A. Inogamov, and M.B. Agranat: *Quant. Electron.*, 44, (2014) 535.
- [14] A.Y. Vorobyev and C. Guo: *Appl. Phys. B.*, 113, (2013) 423.
- [15] T. Y. Hwang, A.Y. Vorobyev and C. Guo: *Appl. Phys. A*, 108, (2012) 299.
- [16] B. Dusser, Z. Sagan, H. Soder, N. Faure, J.P. Colombier, M. Jourlin, and E. Audouard: *Opt. Express*, 18 (2010) 2913.
- [17] J. Bonse, R. Koter, M. Hartelt, D. Spaltmann, S. Pentzien, S. Höhm, A. Rosenfeld and J. Krüger: *Appl. Surf. Sci.*, 336, (2015) 21.
- [18] J. Schroers, T. Nguyen, S. O'Keeffe and A. Desai: *Mater. Sci. Eng., A*, 449-451, (2007) 898.
- [19] W. Zhang, G. Cheng, X.D. Hui and Q. Feng: *Appl. Phys. A*, 115 (2014) 1451.
- [20] U. Kalsoom and S. Bashir: *Appl. Surf. Sci.*, 261, (2012) 101.
- [21] M. Yamaguchi and S. Ueno: *Appl Phys A*, 99, (2010) 23.
- [22] C.A.D. Roeser, A.M.T. Kim, J.P. Callan, L. Huang, E.N. Glezer, Y. Siegal, and E. Mazur, *Rev. Sci. Instrum.*, 74, (2003) 3413.
- [23] D.R. Lide: "CRC Handbook of Chemistry and Physics", ed. by D.R. Lide, (CRC Press, 2009).
- [24] N.A. Inogamov, V.V. Zhakhovsky, and S.I. Ashitkov: *J. Phys., Conf. Ser.* 500, (2014) 112070.
- [25] J.P. Colombier, P. Combis, E. Audouard, and R. Stoian: *New J. Phys.*, 14, (2012) 013039.
- [26] A.E. Siegman and P.M. Fauchet; *IEEE J. Quant. Electronics*, 22, (1986) 1384.
- [27] H. Zhang, J.P. Colombier, C. Li, N. Faure, G. Cheng and R. Stoian: *Phys. Rev. B*, 92, (2015) 174109.
- [28] V. Anantha and A. Taflove: *IEEE Trans. Antennas Propag.*, 50, (2002) 1337.
- [29] S.A. Maier: "Plasmonics: Fundamentals and Applications", ed. by S.A. Maier, (Springer, 2007), p65.
- [30] S.I. Ashitkov, N.A. Inogamov and V.V. Zhakhovskii: *JETP Lett.*, 95, (2012) 176.
- [31] C. Li, G. Cheng, X. Sedao, W. Zhang, H. Zhang, N. Faure, D. Jamon, J. P. Colombier and R. Stoian: *Opt. Express*, 24, (2016) 11558.
- [32] G. Gay and O. Alloschery: *Phys. Rev. Lett.*, 96, (2006) 213901.
- [33] G. Lévêque and O.J.F. Martin: *Phys. Rev. B*, 76, (2007) 155418.

(Received: May 21, 2015, Accepted: September 15, 2016)